

Predicting Crystal Structures and Ionic Conductivities in $\text{Li}_3\text{YCl}_{6-x}\text{Br}_x$ Halide Solid Electrolytes Using a Fine-Tuned Machine Learning Interatomic Potential

Jonas Böhm* and Aurélie Champagne*

Institut de Chimie de la Matière Condensée de Bordeaux, CNRS, 33600 Pessac, France

E-mail: jonas.arnum@gmail.com; aurelie.champagne@icmcb.cnrs.fr

Abstract

Understanding ionic transport in halide solid electrolytes is essential for advancing next-generation solid-state batteries. This work demonstrates the effectiveness of fine-tuning the Crystal Hamiltonian Graph Network (CHGNet) universal machine learning interatomic potential to accurately predict total energies, relaxed geometries, and lithium-ion dynamics in the ternary halide family $\text{Li}_3\text{YCl}_{6-x}\text{Br}_x$ (LYCB). Starting from experimentally refined disordered structures of Li_3YCl_6 and Li_3YBr_6 , we present a strategy for generating ordered structural models through systematic enumeration and energy ranking, providing realistic structural models. These serve as initial configurations for an iterative fine-tuning workflow that integrates molecular dynamics simulations and static density functional theory calculations to achieve near-ab initio accuracy at four orders of magnitude lower computational cost. We further reveal the influence of composition (varied x) on the predicted phase stability and ionic conductivity in LYCB, demonstrating the robustness of our approach for modeling transport properties in complex solid electrolytes.

Introduction

Lithium-ion (Li-ion) batteries play a crucial role in modern energy storage, powering consumer electronics, electric vehicles, and grid-level applications thanks to their high gravimetric energy density and long life cycle. They not only enable the transition toward sustainable mobility but also help stabilize power grids by compensating for the intermittency of renewable energy sources.^{1,2} A conventional Li-ion battery consists of a negative electrode, liquid electrolyte, separator, and positive electrode. In contrast, all solid state batteries (ASSBs), replace the flammable liquid electrolyte and polymer separator with a solid electrolyte (SE), offering enhanced safety, higher energy and power density, faster charging,³ and reduced cross-contamination between electrodes.⁴ However, realizing these advantages introduces major materials and engineering challenges,⁴ including: (1) developing solid composite cathodes that operate reliably under minimal pressure (< 0.1 MPa); (2) identifying SEs with high ionic conductivity, broad electrochemical stability window, mechanical robustness, and low cost; (3) ensuring stable, low-resistance interfaces between SEs and electrodes; and (4) implementing high-capacity anodes such as Li metal or Si-based materials for enhanced battery energy density. Among these, the SE is central, as it governs ion transport, interfacial stability, and mechanical integrity – directly impacting the first three challenges.^{4–6} An ideal SE should combine high ionic conductivity ($\geq 10 \text{ mS cm}^{-1}$), negligible electronic conductivity, mechanical strength sufficient to suppress dendrite growth, and (electro)chemical stability across the 0 – 5 V vs. Li/Li⁺ window.⁴

Recently, ternary metal halides with general formula $\text{Li}_3\text{MA}_{6-x}\text{B}_x$ (M = Y, Er, and In; A, B = Cl, Br, I) have emerged as highly promising SEs.⁷ These materials offer a unique combination of electrochemical stability compatible with 4 V-class cathodes, mechanical and thermal robustness, and room temperature Li⁺ conductivities exceeding 1 mS cm^{-1} .⁷ Their ionic conductivity can be further tuned through compositional substitution and synthesis control,^{7–10} providing a versatile compositional design space for performance optimization.

For instance, van der Maas *et al.* observed in the $\text{Li}_3\text{YCl}_{6-x}\text{Br}_x$ (LYCB) series that ionic conductivity peaks at 5.36 mS cm^{-1} near $x = 4.5$.⁹ They also observed a structural transition from trigonal ($P\bar{3}m1$) to monoclinic ($C2/m$) symmetry around $x = 3$; however the interplay between this structural change and the enhancement in ion transport remains unclear.

Designing halide electrolytes with increased ionic conductivity thus requires a microscopic understanding of how composition, structure, and anion substitution modulate Li^+ migration pathways. Yet, the vast compositional space and experimental limitations in directly probing atomic-scale diffusion processes necessitate integrated computational-experimental approaches. Atomistic modeling, especially molecular dynamics (MD), provides valuable insights into Li^+ diffusion mechanisms and structure-transport relationships, enabling to narrow down the most promising compositions.

The accuracy of MD simulations relies on the description of the underlying potential energy surface (PES), traditionally obtained either from first-principles methods such as density functional theory (DFT) or from empirical force fields. While DFT offers high accuracy, it is computationally prohibitive for the long timescales required to capture diffusion processes (on the order of several nanoseconds). Machine learning interatomic potentials (MLIPs) have recently emerged as a powerful alternative, combining near-DFT accuracy with several orders of magnitude lower computational cost.¹¹ MLIPs approximate the PES by mapping atomic coordinates $[\mathbf{r}_v]$ and atomic numbers $[Z_v]$ to total energies E ,¹² using local environment descriptors and machine learning (ML) regression schemes. Their linear scaling with system size and parallelizability make them ideally suited for large-scale MD simulations.¹³ The performance of an MLIP critically depends on its training data; and large datasets are often required to achieve robust generalization. Pretrained universal machine learning interatomic potentials (uMLIPs) – such as Materials 3-body Graph Network (M3GNet),¹⁴ Crystal Hamiltonian Graph Network (CHGNet),¹⁵ and Scalable EquiVariance-Enabled Neural Network (SEvEnNet)¹³ – are trained on extensive materials databases encompassing diverse chemical systems,^{16–18} and can, in principle, generalize across chemistries. However,

their transferability to new material classes such as halide SEs remains uncertain. Thus, system-specific fine-tuning is often required to achieve reliable quantitative predictions.^{19–22}

In this work, we investigate lithium-ion transport in halide SEs by elucidating how crystal structure, stoichiometry, and anion substitution govern ionic conductivity within the LYCB family. We first present an efficient and accurate enumeration-ranking procedure to systematically explore all possible ordered configurations starting from disordered experimentally-refined structures. We then develop an iterative fine-tuning procedure, inspired by active-learning loops,^{23–26} that integrates targeted DFT data generation with adaptive model refinement. Using this approach, we fine-tune the pretrained CHGNet model¹⁵ to reproduce the PES of LYCB compounds with high-fidelity, enabling nanosecond MD simulations at a computational cost roughly 10^4 times lower than DFT. Finally, we benchmark the fine-tuned CHGNet model against its pretrained counterpart and the state-of-the-art SEvEnNet potential¹³ (pretrained on an even larger dataset including out-of-equilibrium structures¹⁸). Our results provide fundamental insights into Li^+ transport and phase stability across halide compositions, and establishes a general, data-efficient strategy for adapting uMLIP to new material systems – a strategy significantly more effective than training a ML model from scratch. Overall, this framework paves the way for accelerated discovery and rational design of next-generation SEs for ASSBs.

Results and Discussion

Structure enumeration and ground-state identification

A key initial challenge in modeling halide SEs lies in defining suitable starting structures. Experimentally refined models of Li_3YCl_6 (LYC) ($P\bar{3}m1$) and Li_3YBr_6 (LYB) ($C2/m$) exhibit partial occupancies on Li and Y sites, reflecting intrinsic disorder (Figure 1). Determining the lowest-energy ordered configuration among all possible arrangements requires evaluat-

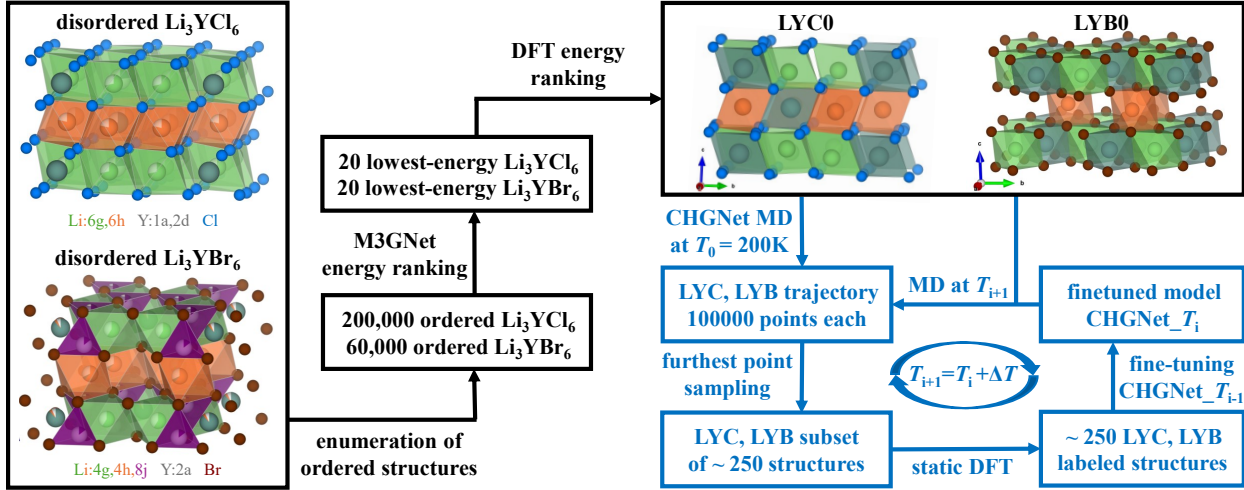


Figure 1: Global workflow combining the enumeration-ranking strategy (black boxes) with the uMLIP fine-tuning framework (blue boxes). Starting from experimentally resolved structures⁸ – which exhibit partial occupancies – symmetry-distinct ordered configurations are enumerated and ranked using the M3GNet uMLIP. Additional DFT calculations are performed on the lowest-energy configurations to identify the ground-state ordered configuration – subsequently used as a starting configuration in the fine-tuning procedure. The fine-tuning procedure involves a series of CHGNet-driven MD simulations (with LAMMPS) at finite temperatures (T_i). For each MD run (1,000,000 steps), DFT calculations (with VASP) are performed on a subset of structures to obtain additional training data and fine-tune CHGNet. Computational details are provided in the Computational Methods.

ing the total energy of thousands of configurations. Conventional Ewald-based electrostatic ranking^{27,28} offers a rapid but approximate criterion that neglects many-body interactions, whereas DFT provides higher accuracy but is computationally prohibitive for such vast configurational spaces. This configurational complexity is not unique to halide conductors and also arises in disordered oxide and sulfide electrodes and electrolytes. Consequently, many of these compounds are absent from large materials databases such as the Materials Project,¹⁶ since their accurate representation demands large supercells and explicit sampling of disorder.

To overcome these limitations, we employ a uMLIP – namely M3GNet model¹⁴ – to efficiently screen and rank candidate configurations. Starting from $1 \times 1 \times 2$ supercells of the experimental LYC and LYB models,⁸ all symmetrically distinct orderings are generated using the *enumlib* library²⁹ (Figure 1). Predicting total energies of the optimized structures

using M3GNet enable us to rank thousands of configurations within an hour, identifying the 20 most stable ones. These are subsequently relaxed using DFT to validate their energetic ordering. This procedure yields physically meaningful low-energy ordered structures for both LYC and LYB, denoted LYC0 ($P\bar{3}c1$) and LYB0 ($C2$), respectively.

We extend this approach to mixed-halide compositions, LYCB, by systematically substituting Cl/Br in both parent lattices, followed by enumeration and M3GNet-based optimization and energy ranking. Across the full composition range ($x = 0$ to 6 , step 0.5), we obtain 13 ordered derivatives for each parent phase. These ordered models provide consistent, low-energy starting points, which we subsequently use in the uMLIPs fine-tuning procedure and for lithium diffusion simulations.

CHGNet performance for energy and volume prediction

To assess baseline performance, we benchmark the pretrained uMLIP CHGNet against DFT reference data.

For 0 K-structures, static CHGNet calculations reproduce energetic trends of LYCB compounds with mean absolute errors (MAEs) below 11 meV atom^{-1} (Figure S1). Furthermore, CHGNet structure optimizations predict volumes and cell parameters within 5% of the DFT values (Figure S4), while being over 2,000 times faster to compute ($\approx 50 \text{ s CPU}$ vs. $\approx 33 \text{ h CPU}$ per structure using DFT). CHGNet’s accuracy for energy and structure predictions at finite temperature is benchmarked in Figure 2. In Figure 2(a), we compare total energies predicted by CHGNet (empty circles) with DFT references (black crosses) for 880 LYC and 880 LYB structures extracted from finite-temperature MD simulations. While CHGNet performs remarkably well at low temperature, energy predictions start to deviate at $T \geq 600 \text{ K}$, with errors in the energy predictions as large as 70 meV atom^{-1} .

To assess CHGNet’s accuracy in volume predictions, we perform MD simulations in the NpT ensemble and obtain equilibrated structures for LYC and LYB up to 650 K. Figures 2(d) and (e) compare CHGNet predicted volumes with SEvEnNet data and available experimental

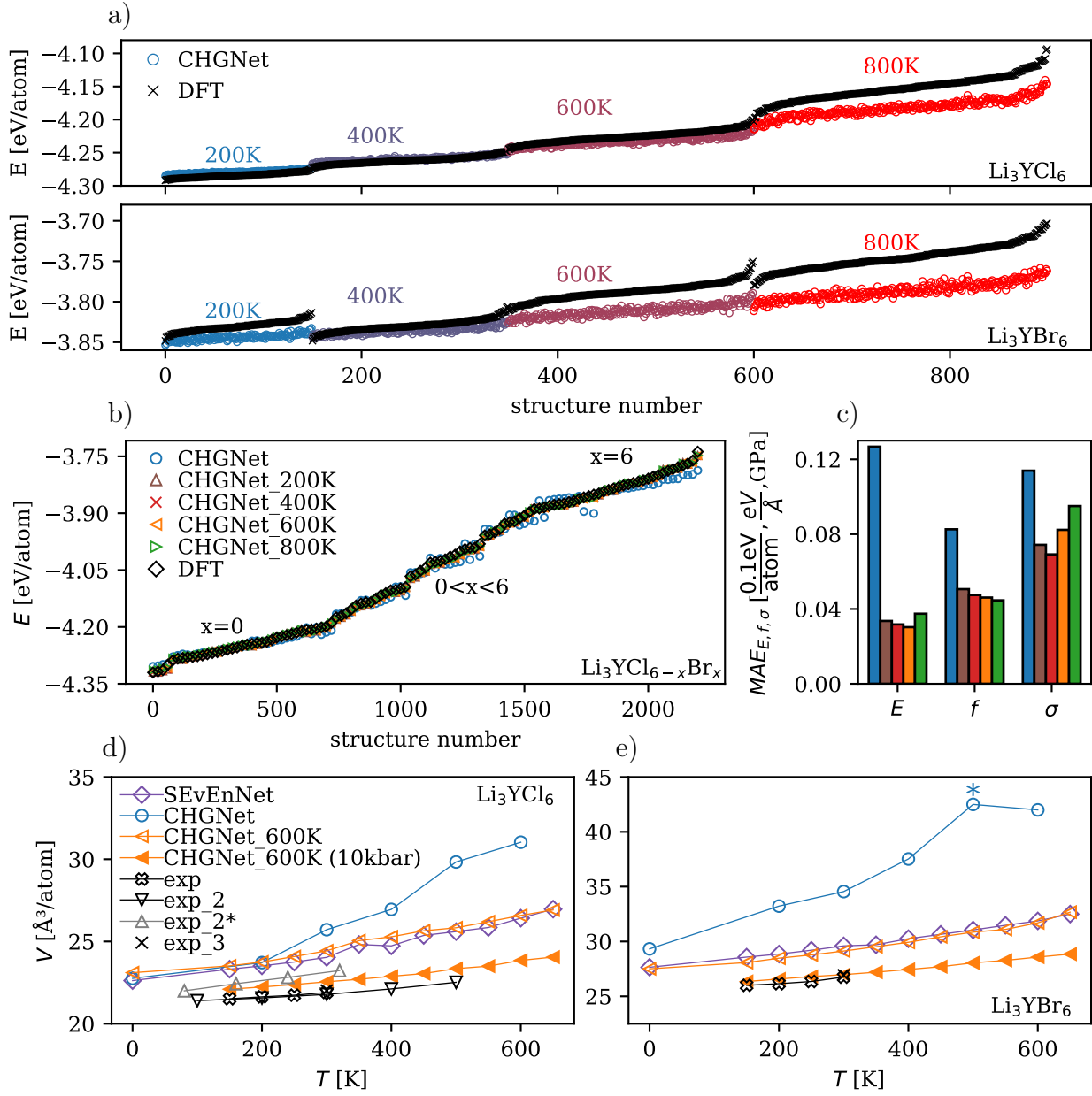


Figure 2: (a) Total energies predicted with CHGNet (colored circles), compared to DFT reference data (black crosses), for a series of finite-temperature structures generated during the fine-tuning procedure in Figure 1. (b) Benchmark of the pretrained and fine-tuned CHGNet potentials for total energy prediction of LYC, LYB, and LYCB, compared to DFT data. (c) MAEs on energy (in $0.1\text{eV}/\text{atom}$), forces (in $\text{eV}/\text{\AA}$), and stress (in GPa). (d) and (e) Average volume/atom resulting from the NpT equilibration MD runs, using the pretrained CHGNet (circles) and fine-tuned CHGNet_600K potentials (empty orange triangles: equilibrated with $p=1\text{ bar}$; solid orange triangles: $p=10\text{ kbar}$), compared to SEvEnNet (purple diamonds),³⁰ and experimental data (black and gray markers) from Refs. 7,8,10. Note the blue star in (e) indicates an unstable simulation with unphysical cell volume, which is scaled by a factor of 10 in the plot.

values: exp (neutron diffraction),⁸ exp_2 (neutron diffraction), exp_2* (synchrotron X-ray diffraction on higher crystalline sample),¹⁰ and exp_3 (X-ray diffraction).⁷ While CHGNet matches SEvEnNet volumes within 2–8% at low temperature, it significantly overestimates volumes at higher temperatures. Moreover, above 500 K, several simulations became unstable, with diverging volume fluctuations. These failure highlight CHGNet’s limitations in capturing thermodynamic and structural diversity encountered at finite temperature, underscoring the need for system-specific fine-tuning.

Fine-tuning CHGNet for finite-temperature stability

To address this, we implement an iterative fine-tuning protocol that augments the training dataset with targeted DFT data for LYC and LYB (see Computational Methods). Four progressively refined models – CHGNet_200K, _400K, _600K, and _800K – are trained by successively incorporating structures from MD trajectories at increasing temperatures (Figures 1 and 2(a)). This active-learning-inspired refinement expands the configurational diversity of the training data and significantly improves agreement with DFT across all metrics, as shown for an independent test-dataset of LYCB structures from 0 K to 800 K in Figures 2(b) and (c). Remarkably, although CHGNet is fine-tuned only on the LYC and LYB endpoints, it retains high predictive accuracy for finite-temperature intermediate compositions. Among all models, CHGNet_600K offers a good balance between the metrics, with energy, force, and stress MAEs below 3.5 meV atom⁻¹, 50 meV Å⁻¹, and 85 MPa, respectively – comparable to state-of-the-art MLIPs.³⁰ Importantly, CHGNet_600K remains stable during long NpT MD runs up to 800 K, where the pretrained model failed. Subsequent analyses are therefore performed using CHGNet_600K, if not otherwise stated.

Fine-tuning also improves performance beyond static energy prediction. Figure 2(d) and Table 1 compare average volumes predicted by CHGNet, CHGNet_600K, and SEvEnNet for LYC. Results for LYB are reported in Figure 2(e) and Table 2. The pretrained model

Table 1: For the LYC system: Predicted volumes (V in $\text{\AA}^3/\text{atom}$) at $T = 0, 200, 300, 400$, and 600 K , activation energies (E_A , in eV), and room-temperature Li conductivities ($\sigma_{300\text{K}}$, in mS cm^{-1}), obtained with CHGNet, CHGNet_600K, and SEvEnNet, and compared to AIMD³¹ and experimental data (extracted from figures in Refs. 7–10).

Models	V [$\text{\AA}^3/\text{atom}$]					E_A [eV]	$\sigma_{300\text{K}}$ [mS cm^{-1}]
	0 K	200 K	300 K	400 K	600 K		
CHGNet (equ. 1 bar)	22.8	23.7	25.7	26.9	31.0	-	-
SEvEnNet (equ. 1 bar)	22.6	23.5	24.0	24.7	26.4	0.17	122
CHGNet_600K (equ. 1 bar)	23.1	23.8	24.4	25.3	26.6	0.12	331
CHGNet_600K (equ. 10 kbar)	-	22.2	22.6	22.9	23.9	0.24	15.7
AIMD ³¹	22.4	-	-	-	-	0.19	14.0
exp ⁸	-	21.6	21.9	-	-	0.411	0.09
exp* ⁸	-	-	-	-	-	0.44	0.06
exp** ⁸	-	-	-	-	-	0.49	0.04
exp_2 ¹⁰	-	21.6	21.8	22.1	-	0.7	0.14
exp_3 ⁷	-	-	22.0	-	-	0.4	0.51
exp_3* ⁷	-	-	-	-	-	0.6	0.04
exp_4 ⁹	-	-	22.0	-	-	0.7	0.05

overestimates volumes by 2-8% at 0 K and up to 25-40% at elevated temperatures, whereas CHGNet_600K achieves agreement within 1% of SEvEnNet predictions and within $\leq 10\%$ of experimental values^{8,10} ($\leq 5\%$ for highly crystalline samples¹⁰). Overall, CHGNet_600K reliably reproduces equilibrium volumes and thermal expansion coefficients (*i.e.* the slope of the curves in Figures 2(d), (e)).

The remaining volume overestimation relative to experiments arises from both the lower crystallinity of experimental samples (compared to ideal simulated crystals) and the known tendency of the PBE functional (used to produce the training data) to overestimate lattice parameters.³² Applying a moderate external pressure of 10 kbar during the MD simulation brings simulated volumes closer to experiment. In subsequent analyses, we perform Li-ion transport simulations in the *NVT* ensemble using two initial configurations: (1) cells equilibrated at 1 bar – representing unconstrained predictive modeling – and (2) cells equilibrated at 10 kbar – yielding volumes closer to experiment and thus more realistic ionic conductivities.

Table 2: For the LYB system: Predicted volumes (V in $\text{\AA}^3/\text{atom}$) at $T = 0, 200, 300, 400$, and 600 K , activation energies (E_A , in eV), and room-temperature Li conductivities ($\sigma_{300\text{K}}$, in mS cm^{-1}), obtained with CHGNet, CHGNet_600K, and SEvEnNet, and compared to AIMD³¹ and experimental data (extracted from figures in Refs. 7–9).

Models	V [$\text{\AA}^3/\text{atom}$]					E_A [eV]	$\sigma_{300\text{K}}$ [mS cm^{-1}]
	0 K	200 K	300 K	400 K	600 K		
CHGNet (equ. 1 bar)	29.3	33.2	34.5	37.5	42.0	-	-
SEvEnNet (equ. 1 bar)	27.6	28.9	29.6	30.2	31.9	0.20	42
CHGNet_600K (equ. 1 bar)	27.5	28.5	29.1	29.9	31.7	0.25	20
CHGNet_600K (equ. 10 kbar)	-	26.6	27.0	27.4	28.6	0.36	0.58
AIMD ³¹	26.9	-	-	-	-	0.28	2.20
exp ⁸	-	26.1	26.8	-	-	0.36	0.3
exp* ⁸	-	-	-	-	-	0.34	1.4
exp** ⁸	-	-	-	-	-	0.21	4.3
exp_3 ⁷	-	-	26.9	-	-	0.37	0.72
exp_3* ⁷	-	-	-	-	-	0.31	1.7
exp_4 ⁹	-	-	-	-	-	0.33	4.7

Lithium-ion diffusion from fine-tuned CHGNet

Using CHGNet_600K, 2 nanosecond-long *NVT* MD simulations are conducted at various temperatures ranging from 400 to 750 K. From these simulations, we quantify Li-ion transport in LYC and LYB, extracting self-diffusion coefficients (D), activation energies (E_A), and room-temperature ionic conductivities ($\sigma_{300\text{K}}$) (Figures 3, 4, and Tables 1, 2).

From the 1 bar-equilibrated cells, we obtain E_A of $0.12 \pm 0.01\text{ eV}$ ($0.25 \pm 0.01\text{ eV}$) and $\sigma_{300\text{K}}$ of $\sim 331\text{ mS cm}^{-1}$ ($\sim 20\text{ mS cm}^{-1}$) for LYC (LYB); shown by empty orange triangles in Figure 3. These values are in the same order of magnitude as the SEvEnNet predictions, and one order of magnitude higher than the ab-initio molecular dynamics (AIMD) values from Ref. 31 (obtained from *NVT* simulations without *NpT* cell equilibration). Using cells compressed to experimental volumes ($p=10\text{ kbar}$, filled orange triangles) reduces Li-ion mobility, yielding E_A of $0.24 \pm 0.01\text{ eV}$ ($0.36 \pm 0.02\text{ eV}$) and $\sigma_{300\text{K}}$ of $\sim 15.7\text{ mS cm}^{-1}$ ($\sim 0.58\text{ mS cm}^{-1}$) for LYC (LYB), in excellent agreement with AIMD. Simulated conductivities for LYC exceed experimental values (obtained from electrochemical impedance spectroscopy at T around 300 K),^{7–10} reflecting the typical overestimation from extrapolating

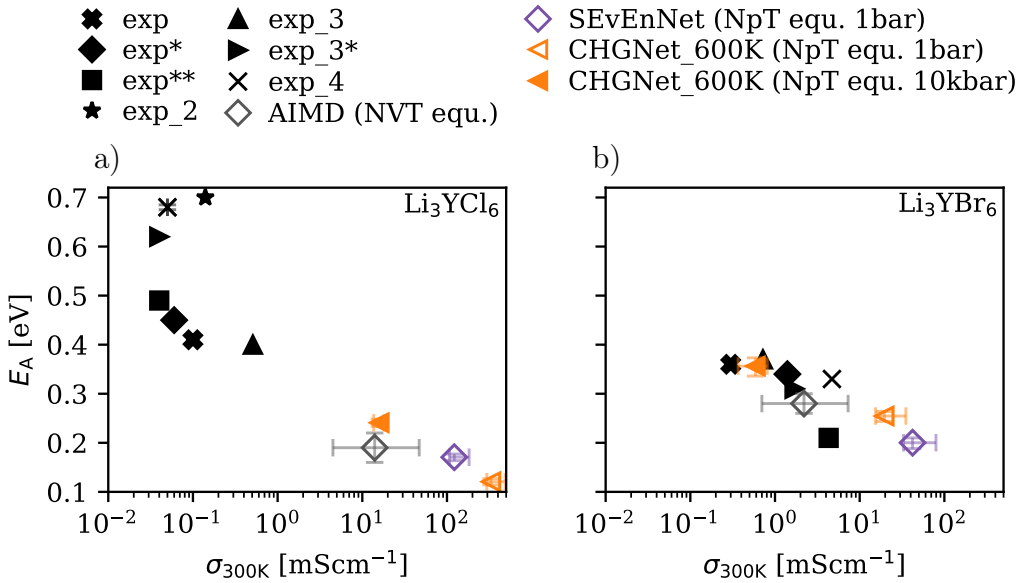


Figure 3: For (a) LYC and (b) LYB, we report the activation energy (E_A) and room-temperature ionic conductivity ($\sigma_{300\text{K}}$), obtained from MD simulations in the *NVT* ensemble, using CHGNet, CHGNet_600K, and SEvEnNet. The simulations were conducted in *NpT*-equilibrated cells under $p=1$ bar (empty orange triangles) and $p=10$ kbar (filled orange triangles). Error bars originate from the variances in the diffusion coefficients that are estimated according to Ref. 33. We compare our predictions to AIMD³¹ and experimental values: exp , exp^* , exp^{**} (*different synthesis);⁸ exp_2 ,¹⁰ exp_3 , exp_3^* (*different synthesis);⁷ exp_4 .⁹

higher-temperature diffusivity to room temperature. This discrepancy aligns with the two diffusion regimes observed experimentally:¹⁰ a high-T regime ($T > 405$ K, $E_A = 0.22$ eV) and a low-T regime ($T < 405$ K, $E_A = 0.7$ eV). For LYB, on the other hand, the CHGNet_600K predictions for the compressed cells and reference AIMD values align well with experiments.

Analysis of mean-squared displacements (MSDs) and diffusivities reveals a clear contrast in the Li-ion transport behavior of LYC and LYB (Figure 4). In LYC, Li^+ diffusion is highly anisotropic, with diffusion coefficients at 500 K about 2 – 3 times larger along the c axis than within the ab -plane (Figures 4(a), (b)). Li^+ probability density maps (Figures 4(c)–(e)) show preferential migration through adjacent face-sharing octahedral sites along c over edge-sharing pathways in the ab -plane, with an intermediate tetrahedral site. This is consis-

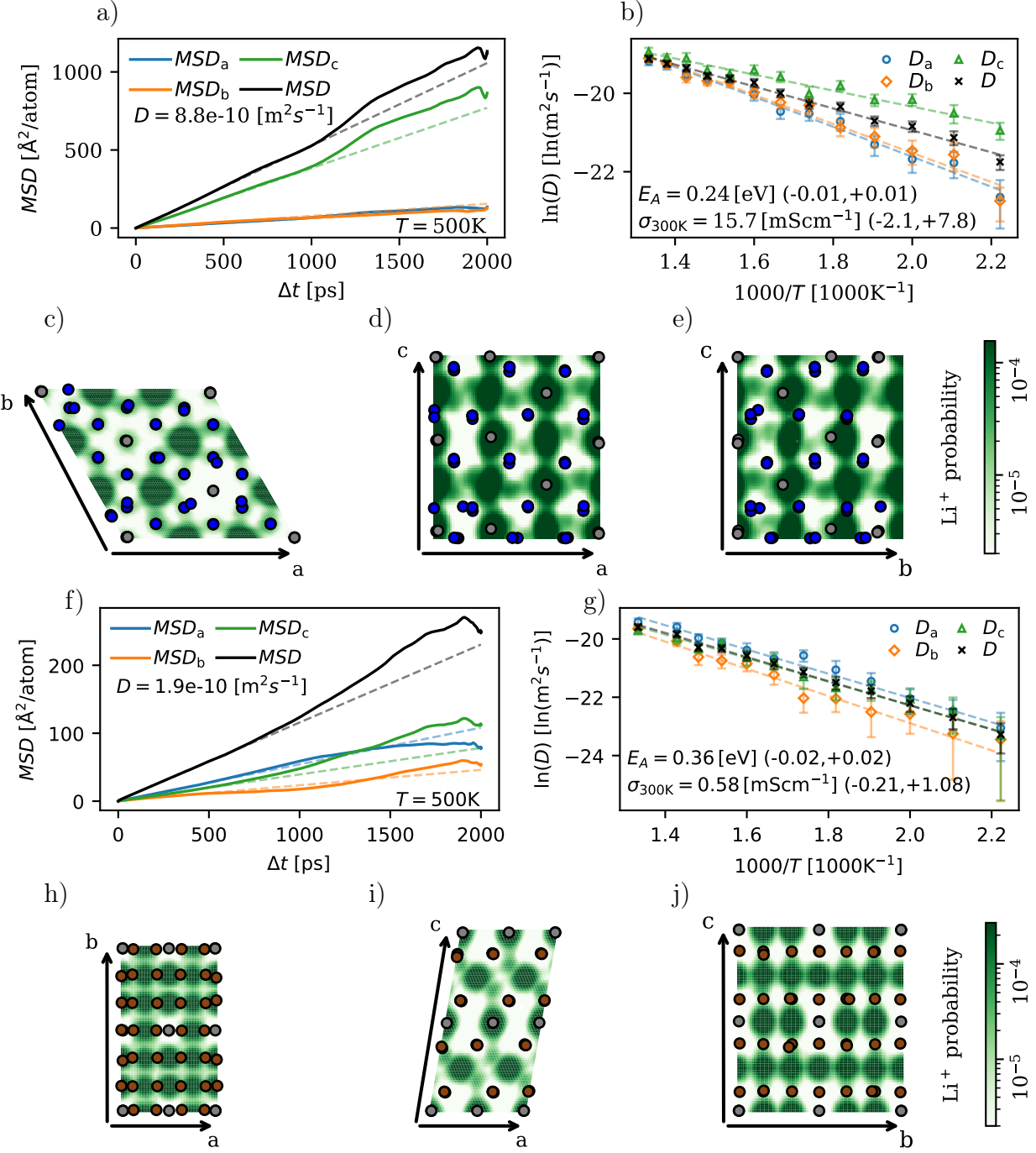


Figure 4: Li⁺ transport properties of (a)-(e) LYC and (f)-(j) LYB, obtained from MD simulations in the *NVT* ensemble, starting from *NpT*-equilibrated structures ($p=10$ kbar), and using the CHGNet_600K potential. (a) and (f) MSD as a function of Δt at $T=500K$; (b) and (g) temperature-dependence of the diffusion coefficient, in logarithmic scale; and (c)-(e) and (h)-(j) Li⁺ probability density maps from MD simulations at $T=500$ K projected on the ab -, ac -, and bc -plane, respectively (Li: green, Y: gray, Cl: blue, Br: brown). Error bars are derived following the procedure in Ref. 33.

tent with the layered structure's open diffusion channels. In contrast, LYB exhibits nearly isotropic diffusion with a diffusion coefficient of $1.9 \times 10^{-10} \text{ m}^2 \text{ s}^{-1}$ at 500 K. This is correlated to the presence of exclusively edge-sharing migration pathways with an intermediate tetrahedral site (Figures 4(f)-(j)).

Effect of halide substitution on phase stability and ion transport

Last, we investigate the impact of Cl/Br substitution on phase stability and Li^+ transport across the mixed LYCB series. The phase stability is assessed from the total energy difference between the two competing phases – trigonal $P\bar{3}c1$ and monoclinic $C2$. Table 3 lists the calculated energy difference, $\Delta E = E_{P\bar{3}c1} - E_{C2}$, for $x = 0$ to 6, as obtained from *ab initio* calculations. Comparable trends are reproduced using CHGNet_600K. The results reveal two nearly degenerate phases, separated by only a few meV/atom, suggesting potential solid-solution behavior at finite temperatures due to thermal contributions. At Br-rich compositions ($x \geq 3$), the monoclinic $C2$ -type phase becomes thermodynamically favored, in agreement with the experimentally observed phase transition within $1.5 < x \leq 3$ reported in Ref. 9.

Table 3: Differences in total energy between the two phases, $\Delta E = E_{P\bar{3}c1} - E_{C2}$ for $x = 0$ to 6, expressed in meV/atom, obtained from *ab initio* calculations. Negative ΔE indicate the $P\bar{3}c1$ phase is energetically favored, whereas positive ΔE mean that $C2$ is more stable.

x_{Br}	ΔE (meV/atom)	x_{Br}	ΔE (meV/atom)
0.0	-2.27	3.5	4.30
0.5	-2.08	4.0	4.51
1.0	-0.82	4.5	4.41
1.5	-0.25	5.0	4.15
2.0	1.79	5.5	4.62
2.5	3.28	6.0	5.22
3.0	3.88		

Figure 5 presents Li^+ transport properties for various LYCB compositions in the crystalline $C2$ space group. With increasing the Cl content (*i.e.*, $x = 6$ down to 3), the room

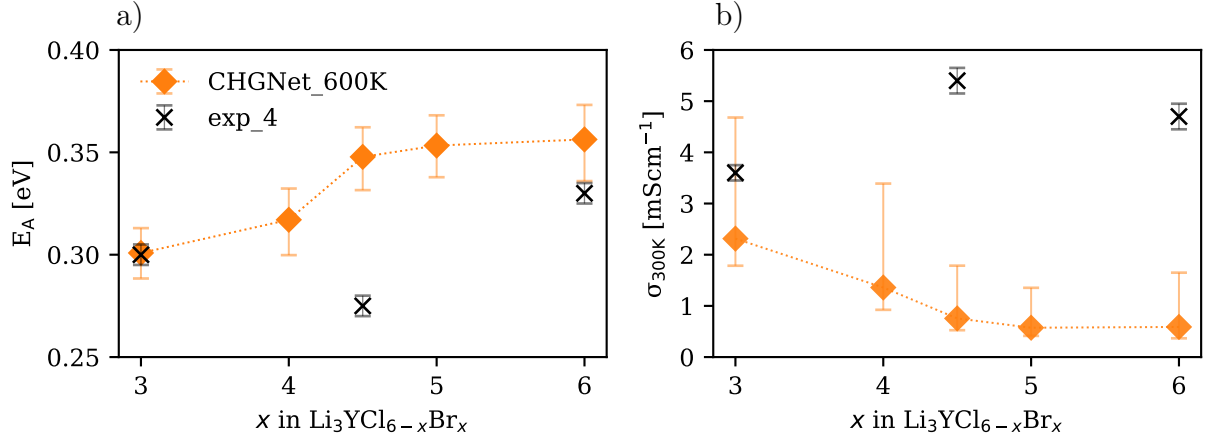


Figure 5: Li^+ transport properties for LYCB obtained from CHGNet_600K MD simulations (starting from NpT -equilibrated structures under $p=10$ kbar), including (a) activation energy E_A and (b) room-temperature ionic conductivity σ_{300K} . We consider $C2$ -symmetry structures of LYCB with $x = 3$ to 6. Experimental values (exp_4⁹) are shown with black crosses.

temperature Li^+ conductivity stays first constant around 0.7 mS.cm^{-1} before rising monotonically within $5.0 \geq x \geq 3.0$. This trend is inversely reflected in the activation energies and could be explained by an increase in disorder and strain within the system that lowers diffusion barriers. Although the experimentally reported conductivity maximum between $x = 3$ and $x = 6$ is not reproduced,⁹ the models predictions are close to the experimental values and highlight that σ_{300K} of LYB can be increased by $\text{Br} \rightarrow \text{Cl}$ substitution. The analysis of MSDs, diffusion coefficients, and Li^+ probability density maps (Figure S5) reveals isotropic transport behavior, not qualitatively different from the LYB system (same space-group $C2$).

Conclusions

In summary, this work establishes a data-efficient and transferable framework for modeling lithium transport in halide SEs by fine-tuning uMLIPs. Starting from experimentally refined disordered structures, we systematically enumerate and rank ordered configurations to identify physically meaningful low-energy models, which are subsequently equilibrated under realistic thermodynamic conditions using MLIP-driven simulations. Fine-tuning the CHGNet model on halide-specific data restores near-DFT accuracy in energy, force, and

stress tensor predictions, stabilized NpT simulations up to 800 K, and enabled nanosecond-scale MD simulations of Li^+ diffusion across the full LYCB composition range.

The fine-tuned CHGNet model achieves quantitative agreement with DFT and AIMD at a cost reduction exceeding four orders of magnitude, while remaining transferable across the full LYCB series. Beyond reproducing known behavior, it reveals key insights such as the anisotropic Li^+ migration pathways in LYC, the isotropic transport in LYB, and the pressure- and composition-dependent modulation of ionic conductivity. More broadly, this work demonstrates that targeted fine-tuning of uMLIPs bridges the gap between efficiency and fidelity, providing a practical route for predictive modeling of complex, partially disordered materials that remain beyond the reach of high-throughput DFT databases. The presented approach thus lays the groundwork for accelerating the discovery and optimization of next-generation SEs through integrated structure–property–transport exploration.

Computational Methods

DFT calculations – DFT calculations are conducted with the Vienna Ab initio Simulation Package (VASP) ^{34,35} using the generalized gradient approximation (GGA) as proposed by Perdew–Burke–Ernzerhof (PBE). ³⁶ For static calculations, a $3 \times 3 \times 3$ Γ -centered k -point grid and a cutoff energy of 350 eV were used, ensuring convergence thresholds of $0.5 \text{ meV atom}^{-1}$. For structure optimizations, a Γ -centered k -point mesh ensuring a 0.2 \AA^{-1} k -point-spacing and cutoff energy of 520 eV are used. Atomic positions and cell parameters are optimized with the FIRE³⁷ optimizer and a convergence threshold of 0.01 eV \AA^{-1} . The same optimizer and threshold are used for MLIP-based structure optimizations.

Structure enumeration and ranking – Starting from the experimental LYC and LYB models,⁸ all symmetrically distinct orderings are generated using *enumlib*.²⁹ Total energy and formation energy are predicted with the *matgl* package,³⁸ using algorithms implemented in ASE³⁹ and different uMLIPs as calculators. M3GNet and CHGNet provide similar en-

ergy predictions, with the former being about 3 times faster – hence M3GNet is used for the ranking procedure here. Structure optimizations are performed using the ASE optimizer, employing the FIRE algorithm and a convergence threshold of $0.01 \text{ eV}\text{\AA}^{-1}$. The results reported herein are generated using the following software versions: Python 3.10.10, Pymatgen 2025.2.18, PyTorch 2.4.0+cu124, ASE 3.23.0, m3gnet 0.2.4, CHGNet 0.3.8 (pretrained model "0.3.0"), sevenn 0.11.0 (pretrained model "SEvEnNet-MF-ompa").

uMLIP-driven MD simulations – MD simulations are performed using the GPU-accelerated LAMMPS package,^{40–46} using either the (finetuned) CHGNet^{15,47} or SEvEnNet-MF-ompa¹³ uMLIP. A timestep of 1 fs is used, with a temperature coupling (NVT , NpT) of 0.1 ps and a pressure coupling (NpT) of 1 ps for the Nosé-Hoover thermostat.^{48,49} Before each NVT MD production run, the following equilibration procedure is carried out: velocities are initialized at 100 K and the system is linearly heated up to the target temperature for 2 ps while keeping the cell parameters fixed. The system is then equilibrated for 50 ps in the NVT ensemble. For the NpT -equilibrated systems, this is followed by a 140 ps equilibration with a target pressure of 1 bar. The equilibrated cell is selected as the one with average cell parameters and volume over the last 112 ps of the NpT -equilibration. The calculation time on a GPU is roughly 0.8 s/atom/picosecond, *i.e.*, more than 10^5 times quicker than a comparable AIMD simulation on a CPU.

uMLIP fine-tuning procedure – The pretrained CHGNet uMLIP is finetuned to enable stable NpT MD simulations at elevated temperatures up to 800 K for LYCB structures. The following iterative procedure is used (Figure 1):

1) Generate structures at finite temperature T_i :

- 1.1)** Starting from LYC0 and LYB0, equilibrate the cell volume with NpT MD at T_i and 1 bar (using CHGNet $_T_{i-1}$), then perform NVT MD (1,000,000 steps; store trajectory every 10th step).
- 1.2)** For each system, derive a subset of structures from the MD trajectory, ensuring a large geometric variety (via furthest point sampling based on the mean squared

error in atom positions)

- 2) Calculate energy, force, and stress labels via static DFT.
- 3) Finetune CHGNet with the labeled dataset including 50% LYC and 50% LYB structures
 - This leads to the fine-tuned CHGNet_{*T_i*}. For this step, the batch size, number of epochs, initial learning rate, and number of frozen layers were optimized; all other parameters were taken from Ref. 15.
- 4) If $T_i < T_{max}$, set $T_{i+1} = T_i + \Delta T$ and jump to step 1.2) for the next iteration.

This methodology ensures that the differences between the perturbed structures that the MLIP encounters during the MD and the structures included in its iteratively expanding training dataset are kept sufficiently small for stable and realistic MD simulations. It is regulated by the parameter ΔT , which was set to 200 K. Step 1) took ~ 0.8 s/atom/picosecond on a GPU; step 3) took $\sim 5 - 10$ minutes on a GPU with a dataset of 150-300 structures per fine-tuning iteration.

Ionic conductivity derivation – From a trajectory of a MD simulation at temperature T for a period t , we derive ion transport properties including atom self-diffusion coefficient, D , ionic conductivity, σ , and activation energy for diffusion events, E_A . First, the averaged atom MSD(Δt) during the time Δt for N atoms i is calculated given:⁵⁰

$$MSD(\Delta t) = \langle |\mathbf{r}(\Delta t)|^2 \rangle = \frac{1}{N} \sum_i \langle |\mathbf{r}_i(t_0 + \Delta t) - \mathbf{r}_i(t_0)|^2 \rangle_{t_0} \quad (1)$$

where Δt stands for a consecutive time interval whose upper bound is the simulation time t , t_0 is a given timestep during the simulation whose upper bound is $t - \Delta t$, brackets $\langle \rangle_{t_0}$ indicate an ensemble average over all possible $t_0 \in [0; t - \Delta t]$. The corresponding lithium self-diffusion coefficient D at temperature T is defined by the Einstein relation:⁵¹

$$D = \lim_{\Delta t \rightarrow \infty} \frac{MSD(\Delta t)}{2d\Delta t} \quad (2)$$

where, d stands for the dimension (e.g., $d = 3$ for 3D diffusion). Based on Eq. 2, D is

derived via a linear fit of discrete $\text{MSD}(\Delta t)$ points. Here, we avoid the ballistic diffusion regime ($0 < \Delta t < x \text{ ps}$) and the region of low Δt sample sizes ($\Delta t > 0.7t$) as recommended in Ref 33. As the observed $\text{MSD}(\Delta t)$ show distinct deviations from a linear correlation around $500 - 1000 \text{ ps}$, Δt_{max} is set to 500 ps . Error bars in the diffusion coefficient are estimated as described in Ref. 33. By sampling several temperatures, E_A is derived via a linear fit of $\ln(D)$ vs. $1/T$, based on the Arrhenius expression:

$$D(T) = \tilde{D} \exp\left(-\frac{E_A}{k_B}T\right). \quad (3)$$

Here, \tilde{D} is the constant diffusion coefficient for $T \rightarrow \infty$. When N atoms (ions) carry a charge q , the ionic conductivity σ can be calculated using the Nernst-Einstein relation:^{51,52}

$$\sigma(T) = \frac{Nq^2}{V k_B T} \cdot D(T) \quad (4)$$

where V is the volume of the system and k_B the Boltzmann constant.

Supporting Information Available

The Supplementary Information is available free of charge.

Acknowledgement

The authors thank Francesco Ricci, Yusuf Shaidu, and Dany Carlier for stimulating discussions, Zhenming Xu for providing additional information on Ref 53, Bassem Sboui for computational support, and Miguel Ceja for support with the Vesta package. The calculations were primarily supported by the computing facilities provided by the Mésocentre de Calcul Intensif Aquitain (MCIA) of the University of Bordeaux. The authors thank the French National Research Agency (STORE-EX Labex Project ANR-10-LABX-76-01) for

financial support.

References

- (1) Daniel, C. Materials and processing for lithium-ion batteries. *JOM* **2008**, *60*, 43–48.
- (2) Goodenough, J. B.; Park, K.-S. The Li-Ion Rechargeable Battery: A Perspective. *Journal of the American Chemical Society* **2013**, *135*, 1167–1176.
- (3) Ohno, S.; Banik, A.; Dewald, G. F.; Kraft, M. A.; Krauskopf, T.; Minafra, N.; Till, P.; Weiss, M.; Zeier, W. G. Materials design of ionic conductors for solid state batteries. *Progress in Energy* **2020**, *2*, 022001.
- (4) Janek, J.; Zeier, W. G. Challenges in speeding up solid-state battery development. *Nature Energy* **2023**, *8*, 230–240.
- (5) Kerman, K.; Luntz, A.; Viswanathan, V.; Chiang, Y.-M.; Chen, Z. Review—Practical challenges hindering the development of solid-state Li-ion batteries. *Journal of The Electrochemical Society* **2017**, *164*, A1731–A1744.
- (6) Pasta, M.; others Energy 2020 roadmap on solid-state batteries. *Journal of Physics: Energy* **2020**, *2*, 032008.
- (7) Asano, T.; Sakai, A.; Ouchi, S.; Sakaida, M.; Miyazaki, A.; Hasegawa, S. Solid Halide Electrolytes with High Lithium-Ion Conductivity for Application in 4 V Class Bulk-Type All-Solid-State Batteries. *Advanced Materials* **2018**, *30*, 1803075.
- (8) Schlem, R.; Banik, A.; Ohno, S.; Suard, E.; Zeier, W. G. Insights into the Lithium Sub-structure of Superionic Conductors Li₃YCl₆ and Li₃YBr₆. *Chemistry of Materials* **2021**, *33*, 327–337, Publisher: American Chemical Society.

(9) van der Maas, E.; Zhao, W.; Cheng, Z.; Famprakis, T.; Thijs, M.; Parnell, S. R.; Ganapathy, S.; Wagemaker, M. Investigation of Structure, Ionic Conductivity, and Electrochemical Stability of Halogen Substitution in Solid-State Ion Conductor $\text{Li}_3\text{YBr}_x\text{Cl}_{6-x}$. *The Journal of Physical Chemistry C* **2023**, *127*, 125–132, Publisher: American Chemical Society.

(10) Liu, Z.; Chien, P.-H.; Wang, S.; Song, S.; Lu, M.; Chen, S.; Xia, S.; Liu, J.; Mo, Y.; Chen, H. Tuning collective anion motion enables superionic conductivity in solid-state halide electrolytes. *Nature Chemistry* **2024**, *16*, 1584–1591.

(11) Wang, G.; Wang, C.; Zhang, X.; Li, Z.; Zhou, J.; Sun, Z. Machine learning interatomic potential: Bridge the gap between small-scale models and realistic device-scale simulations. *iScience* **2024**, *27*, 109673.

(12) Jacobs, R. et al. A practical guide to machine learning interatomic potentials – Status and future. *Current Opinion in Solid State and Materials Science* **2025**, *35*, 101214.

(13) Park, Y.; Kim, J.; Hwang, S.; Han, S. Scalable Parallel Algorithm for Graph Neural Network Interatomic Potentials in Molecular Dynamics Simulations. **2024**, Publisher: arXiv Version Number: 1.

(14) Chen, C.; Ong, S. P. A universal graph deep learning interatomic potential for the periodic table. *Nature Computational Science* **2022**, *2*, 718–728.

(15) Deng, B.; Zhong, P.; Jun, K.; Riebesell, J.; Han, K.; Bartel, C. J.; Ceder, G. CHGNet as a pretrained universal neural network potential for charge-informed atomistic modelling. *Nature Machine Intelligence* **2023**, *5*, 1031–1041.

(16) Jain, A.; Ong, S. P.; Hautier, G.; Chen, W.; Richards, W. D.; Dacek, S.; Cholia, S.; Gunter, D.; Skinner, D.; Ceder, G.; Persson, K. A. Commentary: The Materials Project: A materials genome approach to accelerating materials innovation. *APL Materials* **2013**, *1*, 011002.

(17) Deng, B. Materials Project Trajectory (MPtrj) Dataset. 2023; https://figshare.com/articles/dataset/Materials_Project_Trajectory_MPptrj_Dataset/23713842/2, Artwork Size: 12188168685 Bytes Pages: 12188168685 Bytes.

(18) Barroso-Luque, L.; Shuaibi, M.; Fu, X.; Wood, B. M.; Dzamba, M.; Gao, M.; Rizvi, A.; Zitnick, C. L.; Ulissi, Z. W. Open Materials 2024 (OMat24) Inorganic Materials Dataset and Models. 2024; <https://arxiv.org/abs/2410.12771>.

(19) Liu, X.; Zeng, K.; Wang, Y.; Zhao, T. A Study on the Fine-Tuning Performance of Universal Machine-Learned Interatomic Potentials (U-MLIPs). 2025; <https://arxiv.org/abs/2506.07401>, Version Number: 1.

(20) Huang, X.; Deng, B.; Zhong, P.; Kaplan, A. D.; Persson, K. A.; Ceder, G. Cross-functional transferability in universal machine learning interatomic potentials. 2025; <https://arxiv.org/abs/2504.05565>, Version Number: 1.

(21) Kaur, H.; Della Pia, F.; Batatia, I.; Advincula, X. R.; Shi, B. X.; Lan, J.; Csányi, G.; Michaelides, A.; Kapil, V. Data-efficient fine-tuning of foundational models for first-principles quality sublimation enthalpies. *Faraday Discussions* **2025**, *256*, 120–138.

(22) Radova, M.; Stark, W. G.; Allen, C. S.; Maurer, R. J.; Bartók, A. P. Fine-tuning foundation models of materials interatomic potentials with frozen transfer learning. *npj Computational Materials* **2025**, *11*, 237.

(23) Li, Z.; Kermode, J. R.; De Vita, A. Molecular Dynamics with On-the-Fly Machine Learning of Quantum-Mechanical Forces. *Phys. Rev. Lett.* **2015**, *114*, 096405.

(24) Shapeev, A. V. Moment Tensor Potentials: A Class of Systematically Improvable Interatomic Potentials. *Multiscale Modeling & Simulation* **2016**, *14*, 1153–1173.

(25) Bernstein, N.; Csányi, G.; Deringer, V. L. De novo exploration and self-guided learning of potential-energy surfaces. *npj Computational Materials* **2019**, *5*, 99.

(26) Vandermause, J.; Torrisi, S. B.; Batzner, S.; Xie, Y.; Sun, L.; Kolpak, A. M.; Kozinsky, B. On-the-fly active learning of interpretable Bayesian force fields for atomistic rare events. *npj Computational Materials* **2020**, *6*, 20.

(27) Ewald, P. P. Die Berechnung optischer und elektrostatischer Gitterpotentiale. *Annalen der Physik* **1921**, *369*, 253–287.

(28) Toukmaji, A. Y.; Board, J. A. Ewald summation techniques in perspective: a survey. *Computer Physics Communications* **1996**, *95*, 73–92.

(29) Hart, G. L. W.; Forcade, R. W. Algorithm for generating derivative structures. *Physical Review B* **2008**, *77*, 224115.

(30) Park, Y.; Kim, J.; Kim, J.; Jeon, H.; Han, S. SevenNet_MF_ompa. 2025; https://figshare.com/articles/software/7net_MF_ompa/28590722/7, Artwork Size: 412242578 Bytes Pages: 412242578 Bytes.

(31) Wang, S.; Bai, Q.; Nolan, A. M.; Liu, Y.; Gong, S.; Sun, Q.; Mo, Y. Lithium Chlorides and Bromides as Promising Solid-State Chemistries for Fast Ion Conductors with Good Electrochemical Stability. *Angewandte Chemie International Edition* **2019**, *58*, 8039–8043.

(32) Lejaeghere, K. et al. Reproducibility in density functional theory calculations of solids. *Science* **2016**, *351*, aad3000.

(33) He, X.; Zhu, Y.; Epstein, A.; Mo, Y. Statistical variances of diffusional properties from ab initio molecular dynamics simulations. *npj Computational Materials* **2018**, *4*, 18.

(34) Kresse, G.; Furthmüller, J. Efficient iterative schemes for *ab initio* total-energy calculations using a plane-wave basis set. *Physical Review B* **1996**, *54*, 11169–11186.

(35) Kresse, G.; Joubert, D. From ultrasoft pseudopotentials to the projector augmented-wave method. *Physical Review B* **1999**, *59*, 1758–1775.

(36) Perdew, J. P.; Burke, K.; Ernzerhof, M. Generalized Gradient Approximation Made Simple. *Physical Review Letters* **1996**, *77*, 3865–3868.

(37) Bitzek, E.; Koskinen, P.; Gähler, F.; Moseler, M.; Gumbsch, P. Structural relaxation made simple. *Physical Review Letters* **2006**, *97*, 170201.

(38) Ko, T. W.; Deng, B.; Nassar, M.; Barroso-Luque, L.; Liu, R.; Qi, J.; Liu, E.; Ceder, G.; Miret, S.; Ong, S. P. Materials Graph Library (MatGL), an open-source graph deep learning library for materials science and chemistry. 2025; <https://arxiv.org/abs/2503.03837>, Version Number: 1.

(39) Hjorth Larsen, A. et al. The atomic simulation environment—a Python library for working with atoms. *Journal of Physics: Condensed Matter* **2017**, *29*, 273002.

(40) Thompson, A. P.; Aktulga, H. M.; Berger, R.; Bolintineanu, D. S.; Brown, W. M.; Crozier, P. S.; In 'T Veld, P. J.; Kohlmeyer, A.; Moore, S. G.; Nguyen, T. D.; Shan, R.; Stevens, M. J.; Tranchida, J.; Trott, C.; Plimpton, S. J. LAMMPS - a flexible simulation tool for particle-based materials modeling at the atomic, meso, and continuum scales. *Computer Physics Communications* **2022**, *271*, 108171.

(41) Brown, W. M.; Wang, P.; Plimpton, S. J.; Tharrington, A. N. Implementing molecular dynamics on hybrid high performance computers – short range forces. *Computer Physics Communications* **2011**, *182*, 898–911.

(42) Brown, W. M.; Kohlmeyer, A.; Plimpton, S. J.; Tharrington, A. N. Implementing molecular dynamics on hybrid high performance computers – Particle–particle particle–mesh. *Computer Physics Communications* **2012**, *183*, 449–459.

(43) Brown, W. M.; Yamada, M. Implementing molecular dynamics on hybrid high performance computers—Three-body potentials. *Computer Physics Communications* **2013**, *184*, 2785–2793.

(44) Nguyen, T. D.; Plimpton, S. J. Accelerating dissipative particle dynamics simulations for soft matter systems. *Computational Materials Science* **2015**, *100*, 173–180.

(45) Nguyen, T. D. GPU-accelerated Tersoff potentials for massively parallel Molecular Dynamics simulations. *Computer Physics Communications* **2017**, *212*, 113–122.

(46) Nikolskiy Vsevolod; Stegailov Vladimir *Advances in Parallel Computing*; IOS Press, 2020.

(47) Corporation, A. Customized LAMMPS (2Aug2023) for Neural Network Potential. <https://github.com/advancesoftcorp/lammps>, 2023; Accessed: 2025-05-16.

(48) Nosé, S. A molecular dynamics method for simulations in the canonical ensemble. *Molecular Physics* **1984**, *52*, 255–268.

(49) Hoover, W. G. Canonical dynamics: Equilibrium phase-space distributions. *Physical Review A* **1985**, *31*, 1695–1697.

(50) Ong, S. P.; Mo, Y.; Richards, W. D.; Miara, L.; Lee, H. S.; Ceder, G. Phase stability, electrochemical stability and ionic conductivity of the $\text{Li}_{10\pm 1}\text{MP}_2\text{X}_{12}$ (M = Ge, Si, Sn, Al or P, and X = O, S or Se) family of superionic conductors. *Energy Environ. Sci.* **2013**, *6*, 148–156, Publisher: Royal Society of Chemistry (RSC).

(51) Baktash, A.; Reid, J. C.; Roman, T.; Searles, D. J. Diffusion of lithium ions in Lithium-argyrodite solid-state electrolytes. *npj Computational Materials* **2020**, *6*, Publisher: Springer Science and Business Media LLC.

(52) Evans, D. J.; Morriss, G. P. *Statistical Mechanics of Nonequilibrium Liquids*, 1st ed.; ANU Press, 2007.

(53) Xu, Z.; Duan, H.; Dou, Z.; Zheng, M.; Lin, Y.; Xia, Y.; Zhao, H.; Xia, Y. Machine learning molecular dynamics simulation identifying weakly negative effect of polyanion

rotation on Li-ion migration. *npj Computational Materials* **2023**, *9*, Publisher: Springer Science and Business Media LLC.

Supplementary information

Fine-tuning approach – Training dataset at finite temperatures

Figure 2(a) compares the static DFT energies with corresponding CHGNet predictions for LYC and LYB systems. Structures at 200 K were generated by MD simulations using the pretrained CHGNet, while higher-temperature structures were obtained from MD simulations using the fine-tuned CHGNet from the previous fine-tuning iteration CHGNet $_T_{i-1}$ (see, Figure 1). All MD simulations were conducted in the *NVT* ensemble at the target temperature and ambient pressure, with the simulation cell equilibrated under *NpT* conditions. For LYC, each iteration progressively added structures with higher DFT energies to the fine-tuning dataset, effectively broadening the explored configurational space. For LYB, however, some overlap between energy ranges was observed, particularly at 200 K and 400 K, where the DFT energies fell within a narrow window ($[-3.85; -3.81]$ eV). This indicates that the pretrained model (used at 200 K) could not sufficiently discriminate between structures in this energy range, leading to underestimated potential energies. A smaller temperature step would likely have mitigated this issue. Overall, using this approach, the relevant space of out-of-equilibrium structures is systematically explored, while avoiding highly improbable configurations.

Fine-tuning approach – Transferability across various test datasets

To evaluate the accuracy and transferability of the finetuned versions of CHGNet, several independent test datasets were used.

LYBC equilibrium structures from the enumeration

Although CHGNet was only finetuned on LYB and LYC structures, improved accuracy is expected for energy, force, and stress predictions for mixed-halide LYCB structures. To verify this hypothesis, we generated a test dataset with static DFT data produced for a

subset of LYCB structures obtained from the enumeration in (~ 10 structures per initial spacegroup and per x value). Figure S1(a) shows the DFT energy for these structures and the corresponding predictions of the different CHGNet versions. First, we note that the total energy rises nearly linearly with the degree of substitution (x_{Br}). The energy difference between the structures derived from the two different spacegroups is in the range of a few meV/atom, reflected by small energy step within each plateau. From the MAEs on energy, force, and stress MAEs, reported in Figure S1(b), CHGNet_400 and CHGNet_600 show the best performance.

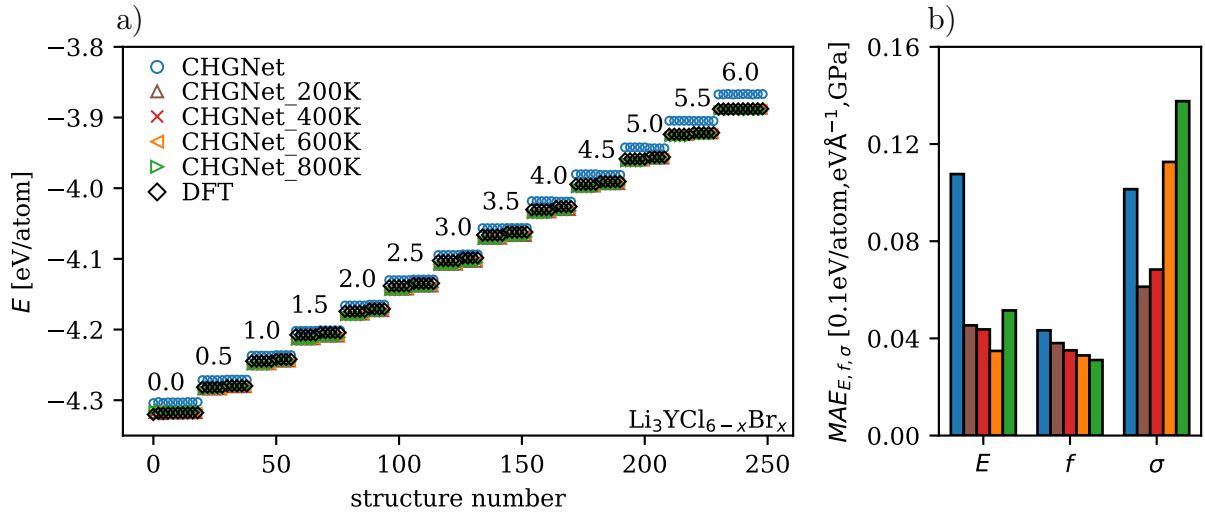


Figure S1: (a) Total energies of LYCB near-groundstate structures from the enumeration-ranking procedure calculated with DFT (black diamonds) and the different CHGNet versions. The number over each energy plateau corresponds to the x value in $\text{Li}_3\text{YCl}_{6-x}\text{Br}_x$. (b) MAEs in energy (in $0.1\text{eV}/\text{atom}$), force (in $\text{eV}/\text{\AA}$), and stress (in GPa) predictions compared to DFT.

Finite-temperature LYC and LYB structures

We further evaluated the accuracy of the CHGNet models against high-temperature structures. Figure S2 shows a similar analysis for an independent test dataset incorporating finite-temperature structures sampled during MD simulations around 300 K-700 K (using CHGNet_600K). For both LYB and LYC, each 50 K, an NpT -equilibration was done, followed by an NVT production run. Using furthest point sampling based on the MAE in

atom positions, 50 structures were extracted from each production trajectory. The complete dataset therefore includes 9×50 structures generated between 300 K and 700 K – a representative testset, with different structures than those included in the finetuning procedure. DFT and CHGNet static energy predictions, shown in Figure S2(a), span a similar energy range compared to the finetuning dataset. Compared to DFT, CHGNet tends to over-predict in the lower energy range and under-predict in the higher energy range, more pronounced for LYB structures. Regarding the MAEs compared to DFT, the finetuned models from higher temperature iterations show better accuracy for this data set (Figure S2(b)). CHGNet_600 K is the best-performing model reaching energy, force, and stress MAEs lower than 2 meV, 50 meV \AA^{-1} , and 60 MPa, respectively.

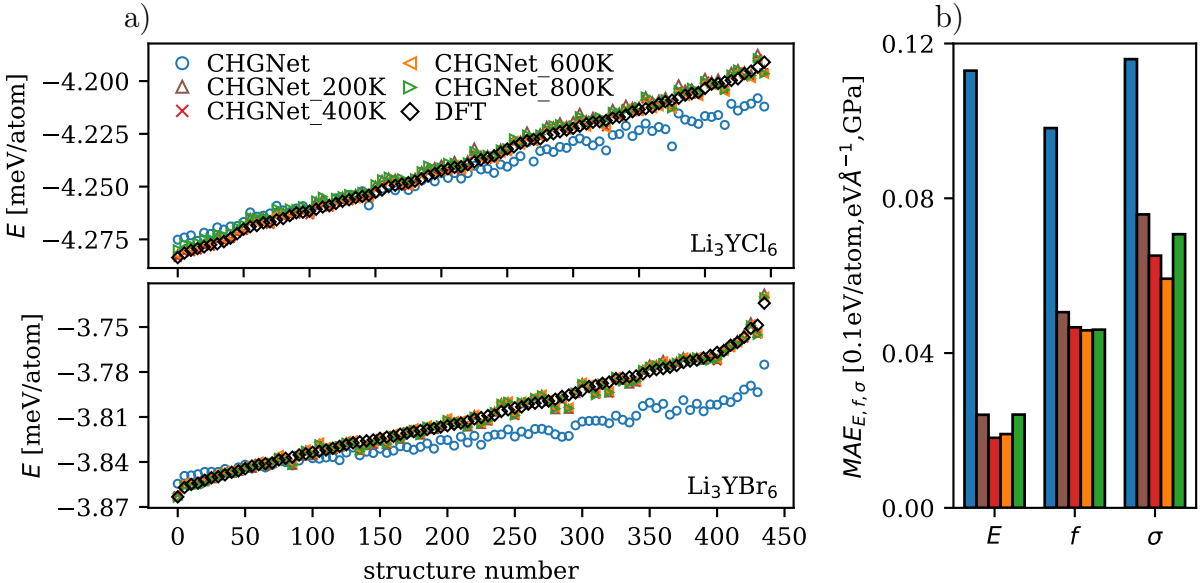


Figure S2: (a) Total energies of finite-temperature LYC and LYB structures from MD trajectories between 300 K and 700 K. They were calculated using DFT (black diamonds) and the different CHGNet versions. (b) Corresponding MAEs in energy (in 0.1eV/atom), force (in eV/ \AA), and stress (in GPa) predictions compared to DFT.

Finite-temperature LYCB structures

A similar analysis was performed with a test dataset obtained from MD trajectories for LYCB with $x \in \{1.5, 3.0, 4.5\}$ at temperatures around 300 K-700 K. MLIP benchmark data

are shown in Figure S3. Here, CHGNet_600 and CHGNet_800 are the best-performing models, with minimal MAEs.

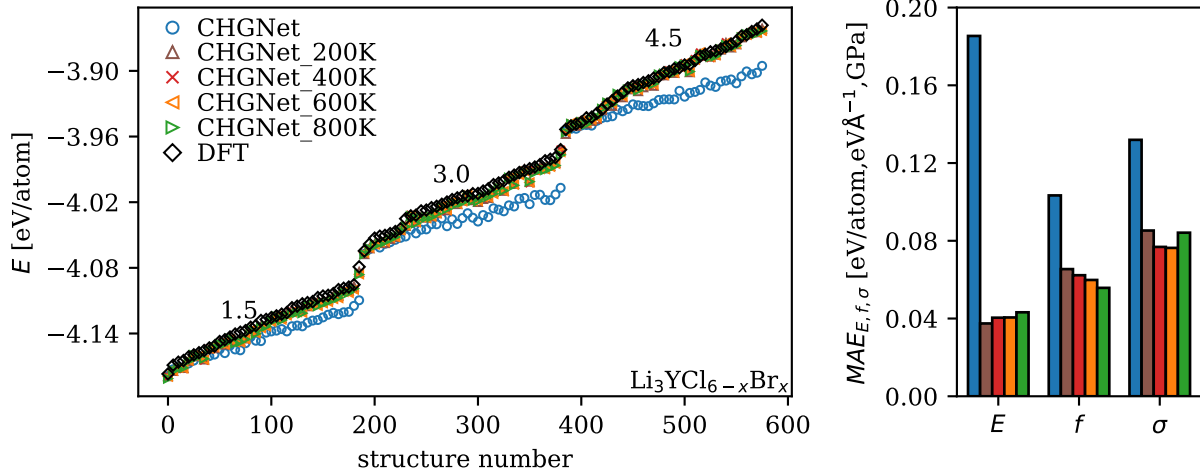


Figure S3: (a) Total energies of LYCB finite-temperature structures from the enumeration-ranking procedure. They were calculated with DFT (black diamonds) and the different CHGNet versions. The number over each energy plateau corresponds to the x value in $\text{Li}_3\text{YCl}_{6-x}\text{Br}_x$. (b) Corresponding MAEs in energy (in 0.1eV/atom), force (in eV/Å), and stress (in GPa) predictions compared to DFT.

Overall, these results show that fine-tuning CHGNet significantly improves accuracy in energy, force, and stress predictions. Across all test datasets considered above, CHGNet_600K provides a good compromise for calculations of equilibrium and finite temperature LYC, LYB, and LYCB structures. The model reaches overall MAEs smaller than 3.5 meV, 50 meVÅ⁻¹, and 85 MPa for energy, force, and stress predictions compared to DFT (see, Figure 2 (b,c)).

Optimization of cell parameters

Figure S4 reports predicted volumes (V), cell parameters (a, b, c), and angles (α, β, γ) predicted with CHGNet and CHGNet_600K, compared to DFT calculations, for the low-energy structures of LYCB (considering two spacegroups: $C2$ and $P\bar{3}c1$) obtained from the enumeration-ranking procedure.

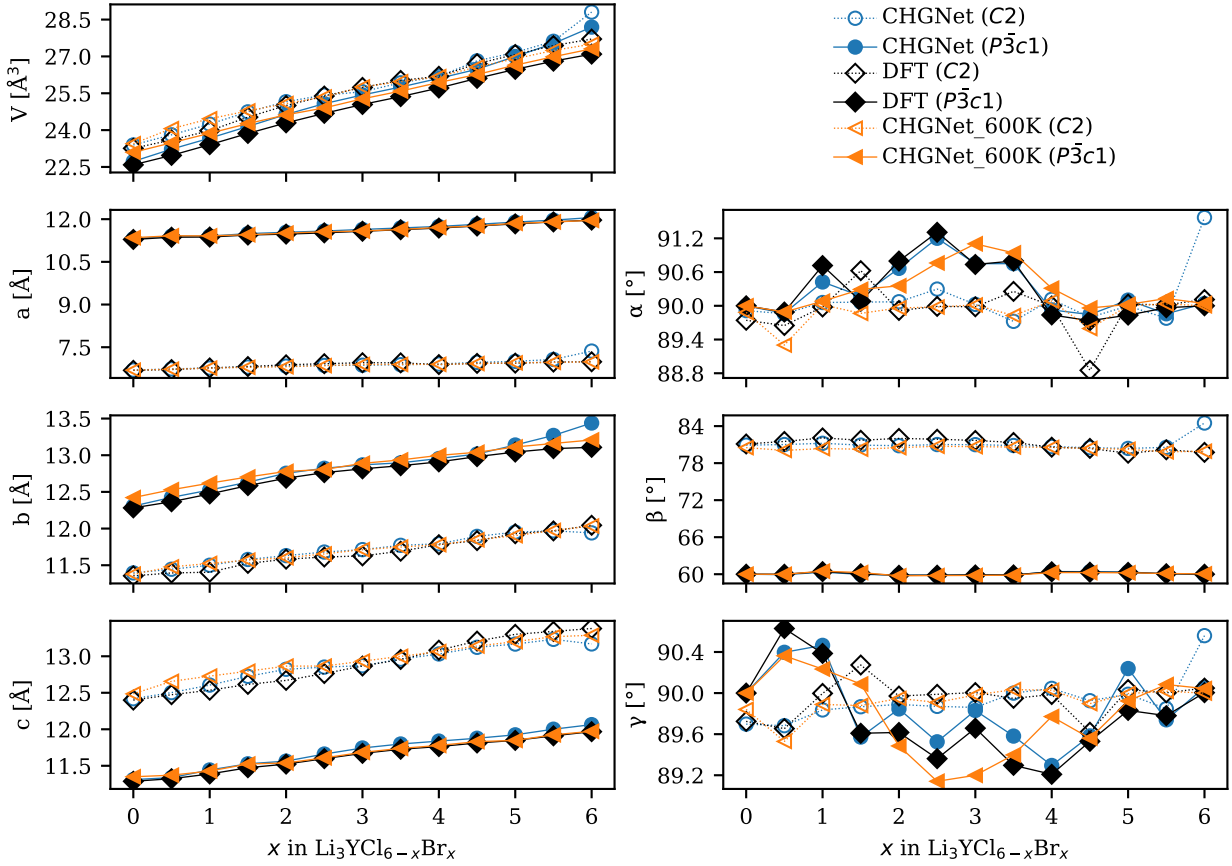
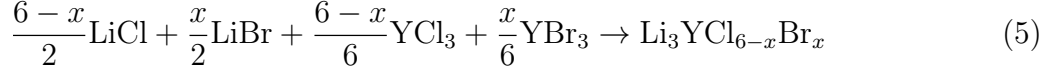


Figure S4: Computed volume/atom and cell parameters ($a, b, c, \alpha, \beta, \gamma$) for the optimized LYCB structures corresponding to the lowest-energy configuration obtained in the enumerations-ranking procedure. Results obtained with DFT, CHGNet, and CHGNet_600K are compared for different x in $\text{Li}_3\text{YCl}_{6-x}\text{Br}_x$. The space group labels $C2$ and $P\bar{3}c1$ refer to the space groups of LYB0 and LYC0 from which the mixed anion structures were derived.

Phase stability prediction based on formation and total energies

Experimentally, mixed-halide LYCB electrolytes have been reported to exhibit two possible polymorphs: trigonal phase ($P\bar{3}m1$) and a monoclinic ($C2/m$) phase, differing mainly by the anionic stacking configurations (hcp for the former, ccp for the later). To perform accurate and realistic simulations of Li-ion transport for these phases, we first assessed the lowest-energy space group and configuration for each mixed-halide composition. Formation energies

were evaluated considering:



Total energy and formation energy differences are reported in Table 3 in the main text. These differ only by a few meV between the two competing phases, suggesting a solid solution at finite temperatures may form (though not observed experimentally yet⁹). Qualitatively, our results indicate that, at $x \geq 3$ in LYCB, the formation of $C2$ LYCB is favored over $P\bar{3}c1$, in agreement with recent experimental observations in Ref. 9.

Li₃YCl₃Br₃ - Lithium-ion diffusion

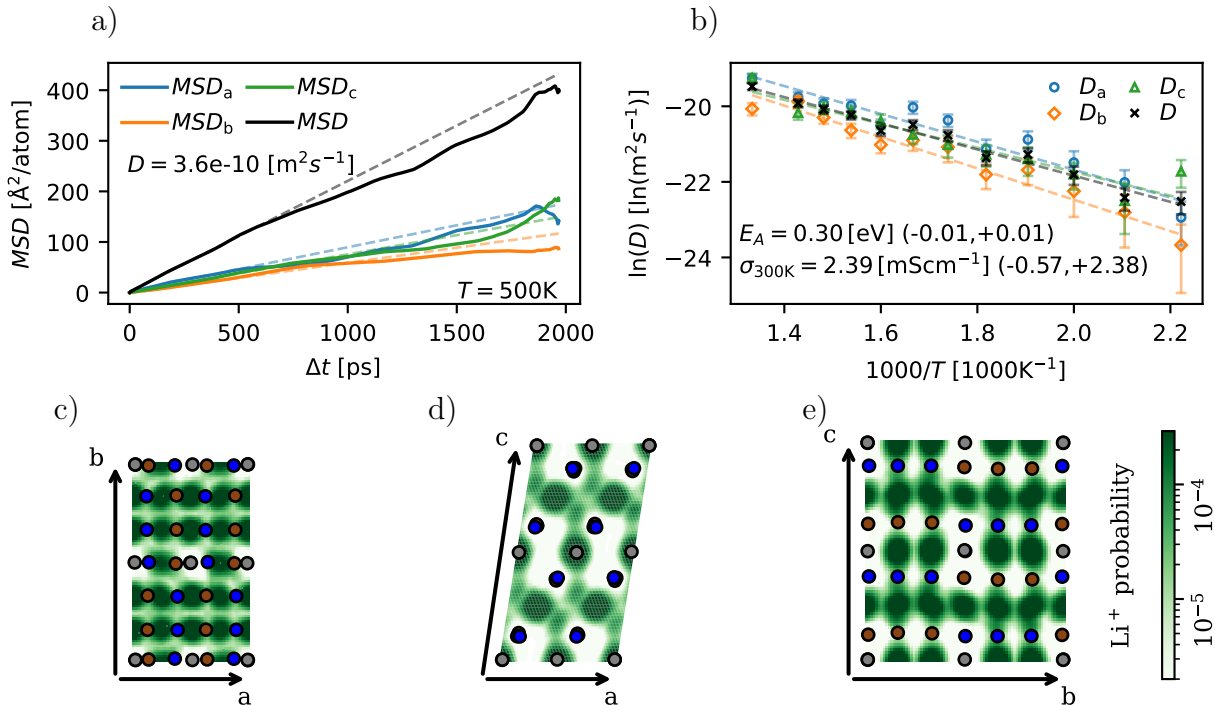


Figure S5: Li⁺ transport properties of LYCB, obtained from MD simulations in the *NVT* ensemble, starting from *NpT*-equilibrated structures (p=10 kbar), and using the CHGNet_600K potential. (a) MSD as a function of Δt at T=500 K; (b) temperature-dependence of the diffusion coefficient, in logarithmic scale; and (c)-(e) Li⁺ probability density from MD simulations at T=500 K projected along \vec{a} , \vec{b} , and \vec{c} on the ab -, ac -, and bc -plane, respectively (Li: green, Y: gray, Cl: blue, Br: brown).